

Quantum Hall effect and semimetallic behavior of dual-gated ABA trilayer graphene

E. A. Henriksen,^{1,*} D. Nandi,¹ and J. P. Eisenstein¹

¹*Condensed Matter Physics, California Institute of Technology, Pasadena, CA 91125*

(Dated: September 5, 2022)

Abstract

The electronic structure of multilayer graphenes depends strongly on the number of layers as well as the stacking order. Here we explore the electronic transport of purely ABA-stacked trilayer graphenes in a dual-gated field effect device configuration. We find both the quantum Hall effect (QHE) and low-field transport to be distinctly different from the mono- and bilayer graphenes, showing electron-hole asymmetries that are strongly suggestive of a semimetallic band overlap. When subject to an electric field perpendicular to the sheet, Landau level splittings due to breaking of the lattice mirror symmetry are clearly observed.

PACS numbers: 73.22.Pr, 73.20.At, 73.43.-f, 73.50.Dn

Single and bilayer graphenes are well known to have low energy electronic dispersions that differ dramatically from the parent compound, graphite [1–3]. With just one more layer, trilayer graphene exhibits two stable stacking configurations with differing electronic structures. In particular, ABA (Bernal)-stacked trilayer graphene is predicted to be a semimetal and is thus the first– and thinnest– multilayer graphene to have a band structure resembling that of bulk graphite [4–9]. Beside providing a look at the behavior of a system that is intermediate between graphite and its fundamental building block of monolayer graphene, study of the electronic transport of ABA graphenes may also shed light on transport anomalies observed in graphite and other semimetals whose properties cannot be so easily varied by external gates [10, 11].

In this work we explore the zero and high magnetic field transport of dual-gated ABA trilayer graphene devices. Trilayer graphene exists in either ABA or ABC-stacked forms, with the latter occurring roughly 15% of the time. This poses a problem for measurements of the QHE where the nature of the edge states may change depending on the stacking type, so that even a small region of ABC stacking can effect the interpretation of transport data. Thus only those graphene flakes identified as ABA trilayers by Fourier transform infrared spectroscopy are utilized here [12]. Moreover as for bilayer graphene, in multilayer graphenes the full range of electronic transport cannot be accessed by a single-side gated device since varying the voltage on just one gate simultaneously changes both the Fermi level (or carrier density n) and the drop in electric potential (or electric displacement field, D) across the layers [13–15]. This problem is remedied by the use of a second (top) gate which allows effects due only to n or D to be separated. In ABA trilayers we find it is crucial to distinguish between the two.

In Fig. 1 (a) an optical microscope image of a $3000\ \mu\text{m}^2$ device is shown, alongside the crystal structure for ABA (or Bernal)-stacked trilayers. The infrared reflectance, R_{tri} , of the entire graphene sheet embedded in this device is shown in Fig. 1 (b), normalized by the reflectance of the substrate, R_{sub} . Two features stand out: a broad minimum centered at $6000\ \text{cm}^{-1}$ and a smaller dip near $4000\ \text{cm}^{-1}$. The former is due to interference effects in the $285\ \text{nm}$ -thick SiO_2 layer [16], while the latter feature arises from transitions to or from the split-off conduction or valence bands as shown schematically inset to Fig. 1 (b). This is similar to the case of bilayer graphene although higher in energy by a factor of $\sqrt{2}$ [17–19]. In conjunction with the lack of any IR signal due to ABC graphene, and with independent confirmation via Raman spectroscopy measurements, this peak at $4000\ \text{cm}^{-1}$ clearly identifies the flake as ABA-stacked trilayer graphene [12].

Graphene-on- SiO_2 samples found to have ABA stacking are fabricated into dual-gated struc-

tures via standard electron beam lithography and thin film deposition techniques. The top gate dielectric is composed of spuncoat PMMA 950K A4 diluted with anisole, and exposed to a 25 kV electron beam at a dosage of $24,000 \mu\text{C}/\text{cm}^2$ to create a hardened dielectric layer. Applying voltages V_b and V_t to the back and top gates leads to changes in both n and D , as given by $n = \alpha (\Delta V_b + \beta \Delta V_t)$ and $D = (D_b - D_t)/2 = (\epsilon_b \Delta V_b / d_b - \epsilon_t \Delta V_t / d_t) / 2$, with $\Delta V_i = (V_i - V_{i0})$. Here the d_i and ϵ_i are the insulating layer thicknesses and dielectric constants, respectively, and the V_{i0} are the offset voltages required to reach $n = D = 0$ due to extrinsic doping. The density and gating efficiency, $\alpha = 7.5 \times 10^{10} \text{ cm}^{-2} \text{ V}^{-1}$, are calibrated by oscillations in R_{xx} at high magnetic fields; while the ratio of the two gate capacitances, β , is determined from the slope, m , of the high-resistance ridge in the zero-field resistivity measurements in Fig. 2 (a) by $-m = 1/\beta = d_t \epsilon_b / (d_b \epsilon_t)$. All electronic transport measurements are made at $T = 0.3 \text{ K}$ using standard low-frequency lockin techniques.

In Fig. 2 we show the sheet resistivity, ρ , at zero magnetic field, B , vs. gate voltages V_t and V_b . Two arrows superimposed on the data define the axes of increasing n and D induced by the two gates, and cross at a saddle point which by symmetry we identify as where $n = D = 0$. This saddle point bears a superficial resemblance to the resistivity of bilayer graphene. Overall, the transport is outlined via profile cuts along the D and n axes, which are plotted for two samples in Fig. 2 (b) as the conductivity, σ , against n (top axis) or D (bottom axis) respectively. As for mono- and bilayer graphenes on SiO_2 , $\sigma \sim n$ away from charge neutrality. At the saddle point, $\sigma_{\min} = 7 - 8e^2/h$ and is 2-3 times greater than for typical bilayer graphene-on- SiO_2 , perhaps due to the higher density of states in trilayer graphene leading to more effective screening of scattering sources [20–22]. The change in σ with increasing D , however, is the most unique feature. Initially σ decreases by a factor of 2 or 3 until $D/\epsilon_0 \approx 0.4 \text{ V/nm}$, beyond which it is flat until for $D/\epsilon_0 > 1.0 \text{ V/m}$ it begins to slowly rise again. This new and unusual behavior—observed in multiple samples—strongly suggests that no gap opens in ABA trilayers at high D . However it is similar to predictions for ABA trilayers subject to an electric potential imbalance between the top and bottom graphene sheets [8].

An earlier work on small dual-gated trilayer devices found entirely different behavior for the resistivity, showing an apparent global *maximum* at the point identified as $n = D = 0$ [23]. However, the nature of the samples used is not clear, as methods to distinguish stacking order were not yet established.

At high magnetic fields, the QHE for ABA trilayer graphene exhibits a number of features

distinguishing it from other graphenes. In Fig. 3 (a) the inverse of the measured Hall resistance, R_{xy}^{-1} , is plotted for $B = 14$ T. Several QH plateaus are clearly visible as wide stripes running from the upper left to lower right. Contour lines drawn at half-integer values of the filling factor, $\nu = nh/eB = \dots -1.5, -0.5, +0.5, +1.5\dots$ serve to emphasize the boundary of each plateau so that, for instance, the -6 plateau is bounded by contours at $\nu = -6.5$ and -5.5 . The most obvious plateaus comprise the sequence of quantum numbers $-14, -10, -6, -2, +6, +10$. The precise quantization, as well as the lack of a plateau at $\nu = +2$, is visible via a profile cut along the line $D = 0$ (dotted line in Fig. 3 (a)) displayed in Fig. 3 (b). A dip in R_{xy}^{-1} near $n = 1 \times 10^{12} \text{ cm}^{-2}$ suggests an incipient plateau, most likely at $\nu = +2$ or $+4$. Most unusually, several distinct plateaus develop near the upper left and lower right corners of Fig. 3 (a), at low n and high values of D . These are highlighted by cuts made along the boundaries of Fig. 3 (a) at constant V_t while varying V_b and vice versa, shown in Fig. 3 (c) and (d) respectively. In each, plateaus at $\nu = +2$ and ± 4 arise symmetrically about the $D = 0$ line, further substantiating our identification of the saddle point as where $n = D = 0$.

A basic ‘1+2’ model of the ABA band structure viewed as a superposition of mono- and bilayer-like bands only partially explains these results [5, 24]. This model is pictured in Fig. 4 (a), with the corresponding zero energy LLs schematically depicted to the right. These are plotted as a function of position so the electron or hole levels diverge up or downward toward the sample edge. In monolayer (bilayer) graphene, one (two) four-fold degenerate LL(s), reflecting the spin and valley degrees of freedom, are found at zero energy. Thus in the ‘1+2’ model, three such levels give rise to a 12-fold degeneracy, yielding quantum numbers $+6$ or -6 when the Fermi level lies where indicated by the dashed lines. Including additional higher energy LLs will, barring accidental degeneracies, lead to the sequence $\dots -14, -10, -6, +6, +10, +14\dots$ which is identical to that observed along the line where $D = 0$ *except* for the -2 plateau.

Analogous to the gap induced in bilayer graphene when lattice inversion symmetry is lifted by a non-zero D , additional QH plateaus are expected from the ‘1+2’ model of ABA trilayer graphene at high D . The mirror symmetry of the ABA lattice is also lifted by an external field, in a way that breaks the degeneracy of the LLs arising from the K and K' valleys in momentum space [4, 24]. Thus a sequence of *two-fold* degenerate LLs is expected at finite D , leading to a “4,2,-2,-4” sequence of QH plateaus much like what is observed in Fig. 3. Since two LLs remain at zero energy, no $\nu = 0$ plateau appears and in fact none has been observed. With further increase of D , further splittings are expected at quantum numbers $\pm 8, \pm 10, \pm 12\dots$. Indeed, in a second sample

at higher D than accessible in Fig. 3, quantized plateaus at $+8$ and $+12$ have been seen.

While the ‘1+2’ model serves to explain most of the QH plateaus at zero and finite D in Fig. 3 (a), it offers no insight into the presence at $D = 0$ of the robust -2 plateau or the corresponding lack of one at $\nu = +2$. The $\nu = -2$ plateau must arise from a splitting of the three zero energy LLs. While in principle many-body interactions can be responsible, in these low mobility samples ($\mu \sim 4000 \text{ cm}^2/\text{Vs}$) disorder is expected to overwhelm interactions. Therefore, we seek an explanation for the -2 plateau in terms of a more accurate model of the trilayer band structure.

In Fig. 4 (b) the ABA band structure is calculated to higher order, using the full set of tight-binding parameters in the Slonczewski-Weiss-McClure model for graphite, with $D = 0$ [1, 8]. In this picture, the mono- and bilayer-like bands become gapped as well as offset from zero energy, leading to the overlap of one approximately linear hole band with a nearly parabolic electron band. The region of overlap delimits the semimetal: at charge neutrality, *both* bands are partially occupied and contribute to transport.

The lowest energy LLs for the higher order calculation are plotted on the right of Fig. 4 (b) as two-fold degenerate levels (for electron spin), with one (two) arising at each extrema of the mono (bi) layer-like bands. Some surprising features appear: new gaps develop at $\nu = -2$, $+2$, and $+4$, and a LL crossing naturally arises as the levels diverge at the sample edge. Thus the higher order model can account for the observation of a plateau at $\nu = -2$. But why then are plateaus absent at $\nu = +2$ and $+4$? In fact the dip in R_{xy}^{-1} identified earlier in Fig. 3 (b) may signal the formation of either the $\nu = +2$ or $+4$ state. Instead, the energy gaps in Fig. 4 (b) may differ in size and be washed out, since the LL energies are sensitive to changes of the tight-binding parameters and these are not well known for trilayer graphene. Indeed, values found for ABA trilayers in a recent work give the same qualitative band structure as Fig. 4 (b), but with the $\nu = +4$ gap reduced by half and the $\nu = \pm 2$ gaps increased by $\sim 50\%$ [25]. However, the position dependence of the LL energies shown in Fig. 4 (b) suggests an intriguing explanation for the robust appearance of the -2 plateau in contrast to the lack of one at $+2$: since at $\nu = +2$ a LL crossing exists near the sample edge, counter-propagating edge modes may lead to an increase in backscattering which spoils the quantization [26, 27].

As the LL sequence and electron-hole asymmetry in the center of Fig. 3 (a) are both consistent with a semimetallic band overlap in ABA trilayers, it is natural to assume that low-field measurements will also show semimetallic transport. To address this, the low-field Hall coefficient, $R_H = dR_{xy}/dB$, and magnetoresistance, ρ_{xx} , are compared to a control sample of monolayer

graphene. The results are shown in Fig. 5 (a) and (b) for trilayer and monolayer samples, respectively, where R_H vs. n is plotted along with the sheet resistivity, ρ . The trilayer data was acquired along $D = 0$, possible only in dual-gated samples. The evolution of R_H is quite different for the two systems. The monolayer data are perfectly symmetric about $n = 0$, and due to disorder do not diverge but rather smoothly change sign over a narrow region of low densities. In contrast, the trilayer data are strongly asymmetric, having a large positive peak at $n = 0$ and a zero crossing at slightly more than $n = 10^{12} \text{ cm}^{-2}$, followed by a weak minimum and slow decrease back toward zero. Meanwhile in ABA trilayers, a $\rho_{xx} \sim B^2$ behavior is observed, characteristic of two-band conduction. This, along with analysis of the clear two-band signatures in the Shubnikov-de Haas oscillations, will be discussed elsewhere.

The differing behavior of R_H can be qualitatively understood in terms of semimetallic transport. The monolayer data are well described by $R_H = -1/ne$ except at the lowest densities, which are modeled by convolving R_H with a Gaussian whose variance, δn , represents a spread of densities due e.g. to electron-hole puddles [14, 28]. While this certainly oversimplifies the role of disorder, a reasonable fit to the data can be found for $\delta n = 0.8 \times 10^{11} \text{ cm}^{-2}$. In contrast, the transport properties are qualitatively different when two bands are occupied. In particular, when electron and hole bands overlap the low-field Hall coefficient becomes [29]

$$R_H = \frac{1}{e} \frac{p - n (\mu_e/\mu_h)^2}{\left(p + n \frac{\mu_e}{\mu_h}\right)^2}, \quad (1)$$

where p and n are the hole and electron densities and μ_e/μ_h is the ratio of their mobilities. Sharply differing from the behavior for a single band, R_H will in general cross zero away from charge neutrality ($p = n$), and at this crossing the ratio of the densities is given by $p/n = (\mu_e/\mu_h)^2$.

In Fig. 4 (b) the number of bands— and associated mobilities— changes several times as the Fermi level is varied. To model R_H , the simplified band structure shown in Fig. 5 (c) is adopted. Depending on the Fermi level position, the relevant one or two band expressions are employed and the result is smoothed with a Gaussian using $\delta n = 3 \times 10^{11} \text{ cm}^{-2}$. Obviously these results will vary with the choice of mobilities and band offsets, but overall the behavior of this model can be summarized by the curves in Fig. 5 (d). There R_H vs. n is calculated for three ratios, $\mu_l/\mu_p = 3.3, 1$, and 0.3 , where μ_l and μ_p are mobilities of the linear and parabolic bands irrespective of the sign of the carriers. Interestingly, the data are best approximated when $\mu_l > \mu_p$, which gives the only curve that captures the pronounced asymmetry of the data and crosses zero at a positive carrier density. Of course, the many choices of band edge offsets and curvatures, combined with

the likely density-dependent mobilities all prohibit using this model to make accurate fits to the data. In particular, substrate-induced potential fluctuations are ubiquitous in SiO₂-based devices and likely to contribute to a smearing of transport effects over a range of densities [3, 30]. Yet these results, in concert with the clear asymmetry of the quantum Hall effect, strongly suggest that ABA trilayer is indeed a semimetal with an unusual LL structure at low energies.

* Electronic address: erikku@caltech.edu

- [1] A. H. Castro Neto *et al.*, *Rev. Mod. Phys.* **81**, 109 (2009).
- [2] D. S. L. Abergel *et al.*, *Adv. Phys.* **59**, 261-482 (2010).
- [3] S. Das Sarma, S. Adam, E. H. Hwang, E. Rossi, *Rev. Mod. Phys.* **83**, 407-470 (2011).
- [4] S. Latil, L. Henrard, *Phys. Rev. Lett.* **97**, 036803 (2006).
- [5] F. Guinea, A. H. Castro Neto, N. M. R. Peres, *Phys. Rev. B* **73**, 245426 (2006).
- [6] B. Partoens and F. M. Peeters, *Phys. Rev. B* **74**, 075404 (2006).
- [7] M. Aoki, H. Amawashi, *Solid State Comm.* **142**, 123-127 (2007).
- [8] M. Koshino, E. McCann, *Phys. Rev. B* **79**, 125443 (2009).
- [9] N. B. Brandt, S. M. Chudinov, Ya. G. Ponomarev, *Semimetals: Graphite and its Compounds*, (North-Holland, Amsterdam, 1988).
- [10] H. Yaguchi, J. Singleton, *J. Phys: Cond. Mat.* **21**, 344207 (2009).
- [11] K. Behnia, L. Balicas, Y. Kopelevich, *Science*, **317**, 1729 (2007).
- [12] C. H. Lui, *et al.*, *Nano Lett.* **11**, 164 (2011).
- [13] Y. Zhang *et al.*, *Nature* **459**, 820 (2009).
- [14] E. A. Henriksen, J. P. Eisenstein, *Phys. Rev. B* **82**, 041412(R) (2010).
- [15] A. A. Avetisyan, B. Partoens, F. M. Peeters, *Phys. Rev. B* **80**, 195401 (2009).
- [16] Z. Li, *et al.*, *Nature Phys.* **4**, 532-535 (2008).
- [17] K. F. Mak, M. Y. Sfeir, J. A. Misewich, T. F. Heinz, *Proc. Nat. Acad. Sci.* **107**, 14999-15004 (2010).
- [18] Z. Li, *et al.*, *Phys. Rev. Lett.* **102**, 037403 (2009).
- [19] A. Kuzmenko, A., *et al.*, *Phys. Rev. B* **79**, 115441 (2009).
- [20] S. Xiao, *et al.*, *Phys. Rev. B* **82**, 041406(R) (2010).
- [21] S. Yuan, H. De Raedt, M. I. Katsnelson, *Phys. Rev. B* **82**, 235409 (2010).
- [22] H. Min, P. Jain, S. Adam, M. D. Stiles, *Phys. Rev. B* **83**, 195117 (2011).

- [23] M. F. Craciun, *et al.*, *Nature Nanotech.* **4**, 383-388 (2009).
- [24] M. Koshino, E. McCann, *Phys. Rev. B* **81**, 115315 (2010).
- [25] T. Taychatanapat, K. Watanabe, T. Taniguchi, P. Jarillo-Herrero, *Nat. Phys.* **7**, 1-5 (2011).
- [26] D. Abanin, *et al.*, *Phys. Rev. Lett* **98**, 196806 (2007).
- [27] H. Fertig, L. Brey, *Phys. Rev. Lett.* **97**, 116805 (2006).
- [28] J. Martin, J., *et al.*, *Nat. Phys.* **4**, 144-148 (2007).
- [29] A. C. Beer, *Galvanomagnetic Effects in Semiconductors* (Academic Press, New York, 1963).
- [30] E. H. Hwang, E., S. Das Sarma, *Phys. Rev. B* **82**, 081409(R) (2010).

Acknowledgments: We gratefully acknowledge conversations with S. Adam, J. Alicea, D. Bergman, B. Chikering, K. C. Fong, M. Koshino, C. H. Lui, A. MacDonald, and E. McCann. Special thanks are due G. Rossman for the use of his spectroscopy lab. This work is supported by the NSF under grant No. DMR-0552270, and the DOE under grant No. DE-FG03-99ER45766.

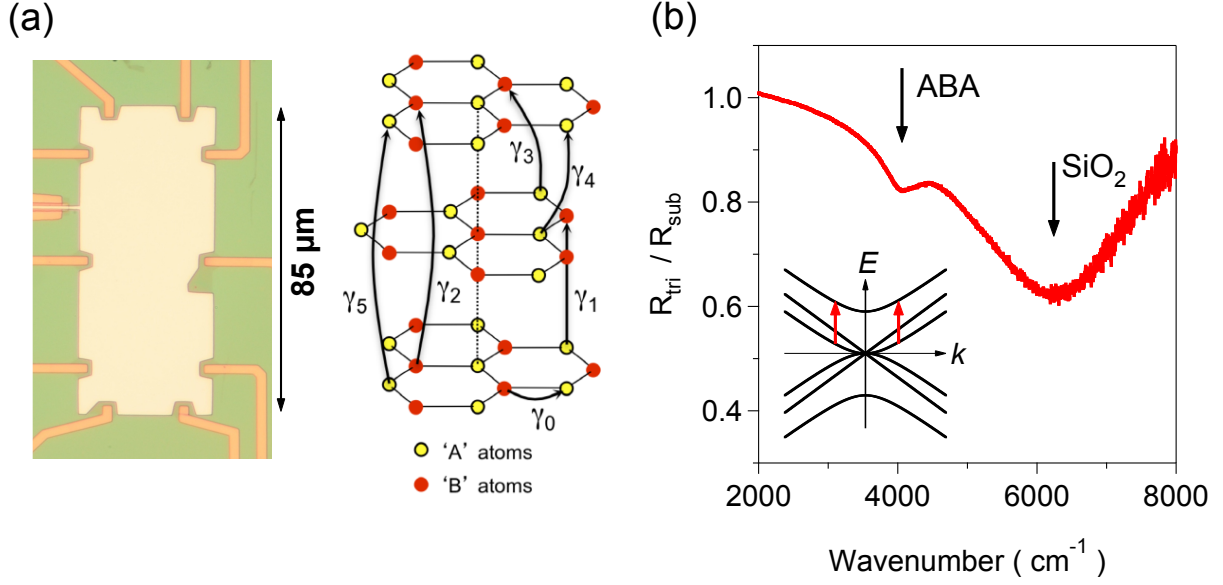


FIG. 1: (Color) (a) Optical image of $3000 \mu\text{m}^2$ dual-gated ABA trilayer graphene device, and crystal structure of ABA (Bernal)- stacked trilayer graphene with arrows indicating the tight-binding hopping parameters in the Slonczewski-Weiss-McClure model [8, 9]. (c) Infrared reflectance, R_{tri} , of the trilayer flake shown in (a) normalized to the substrate reflectance, R_{sub} . The dip near 4000 cm^{-1} is due to transitions to or from the split off bands, shown schematically for the conduction band in the lower left inset, while the larger dip at 6000 cm^{-1} is due to interference in the SiO_2 [16].

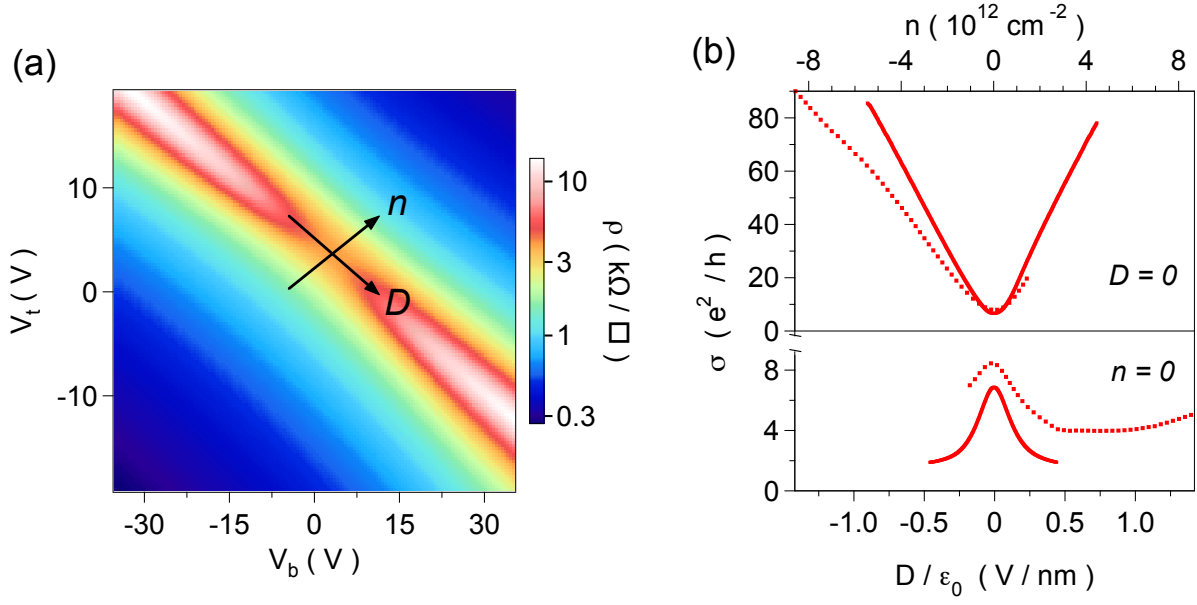


FIG. 2: (Color) (a) ABA trilayer resistivity vs. the top and back gate voltages, V_t and V_b . The arrows at the saddle point indicate the axes of increasing carrier density, n , and electric displacement field, D . (b) Profile cuts along the n and D axes from two samples are plotted as the conductivity, σ , vs. n or D . Solid lines are from Fig. 2 (a), while the dashed lines are from a second sample with a saddle point offset from $V_b = V_t = 0$ due to disorder, so a larger range of D is accessible.

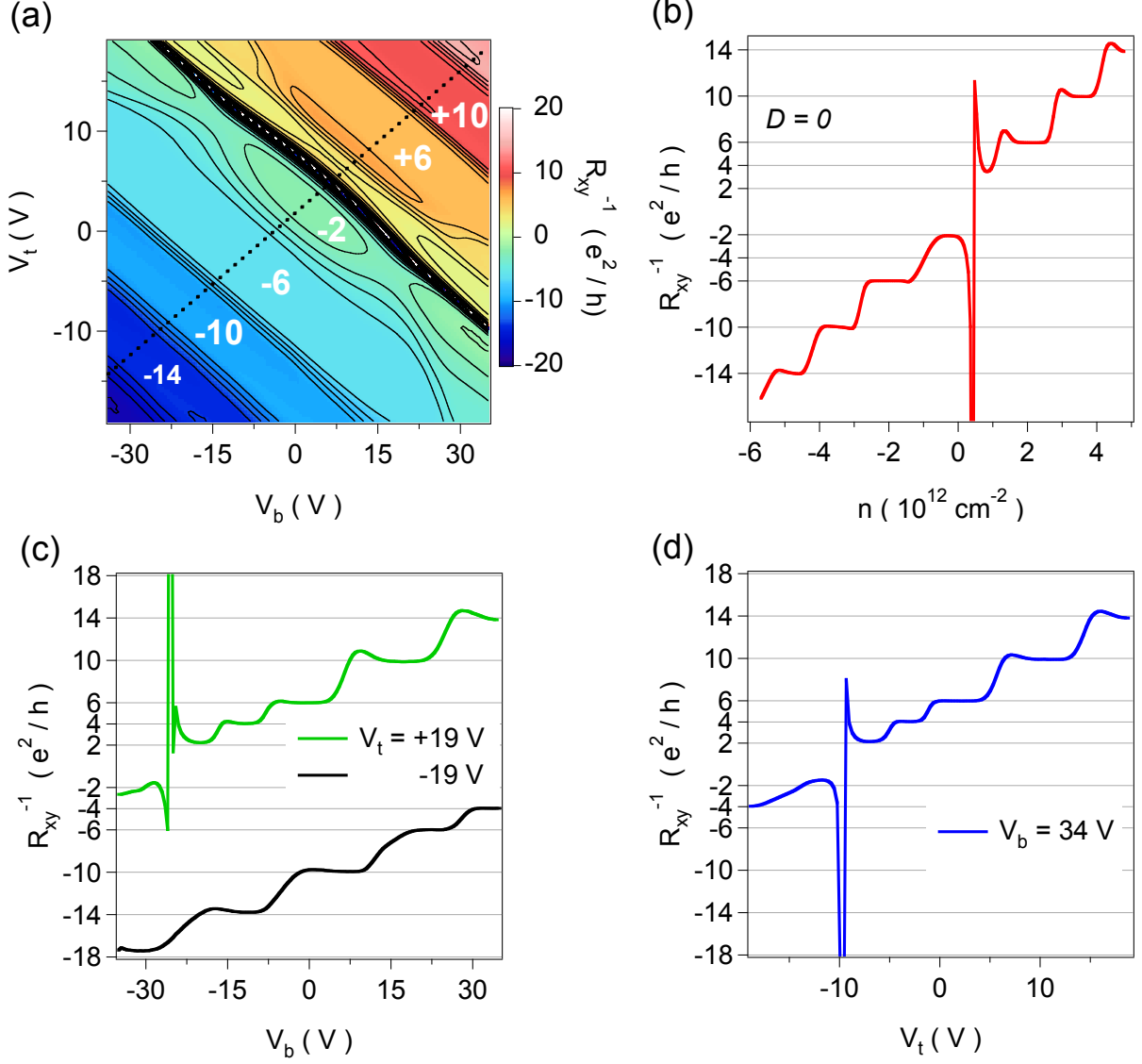


FIG. 3: (Color) (a) Inverse Hall resistance, R_{xy}^{-1} vs. V_b and V_t at $B = 14 \text{ T}$. Contour lines are drawn at filling factors $\nu = \dots -1.5, -0.5, +0.5, +1.5 \dots$. The quantum numbers of several plateaus are indicated in white. Profile cuts through the data are shown in (b), along $D = 0$, indicated by the dashed line; (c) at constant top gate voltages along the top and bottom edges of (a); and (d) along the right edge of (a).

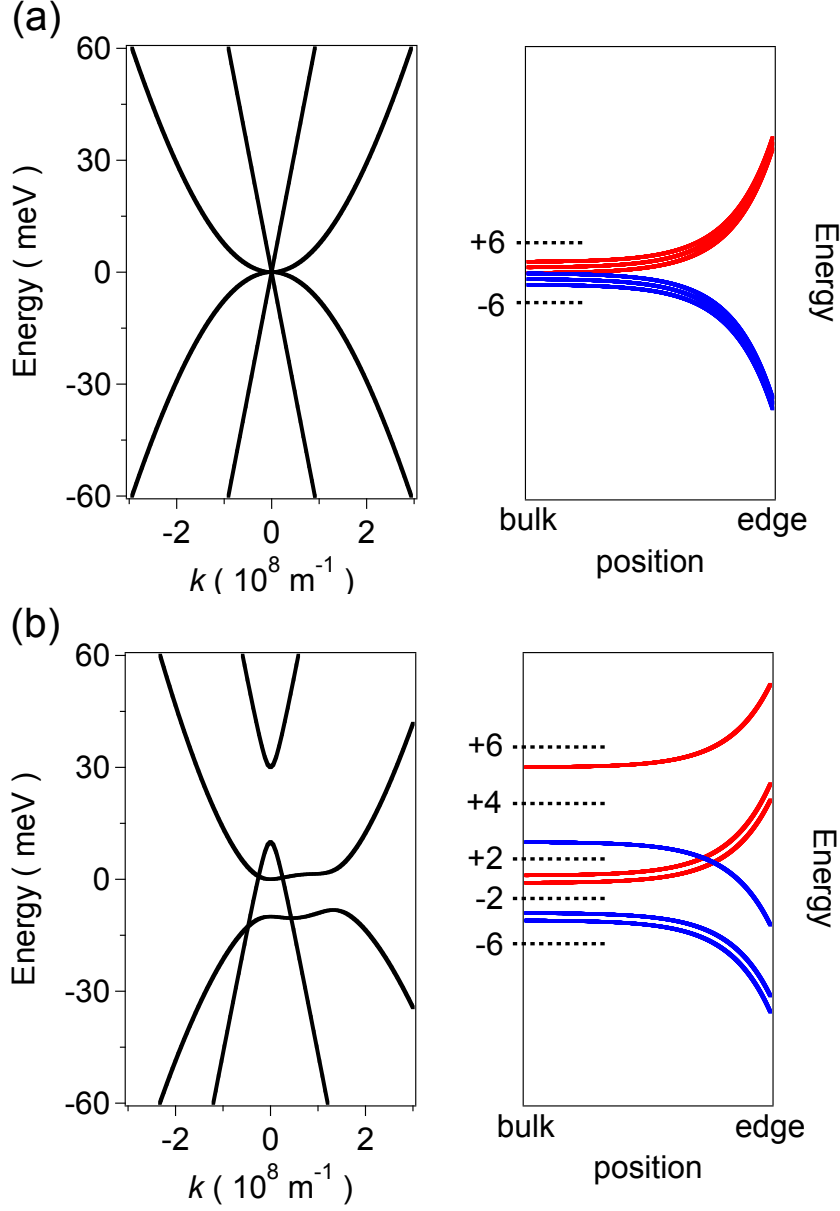


FIG. 4: (Color) (a) The ‘1+2’ band structure and associated zero energy LLs. QH plateaus occur when the Fermi level lies at the dashed lines: $+6$ (-6) when all levels are full (empty). (b) Band structure calculated to higher order (see text). Two bands overlap at zero energy, creating a semimetal. To the right, the corresponding lowest LLs allow QH plateaus at -2 , $+2$, and $+4$. Level energies are plotted against position, diverging up (down) ward for electron (hole) states near the sample boundary. All LLs are two-fold degenerate (for electron spin). Closely spaced pairs mark the number of levels, not additional splittings.

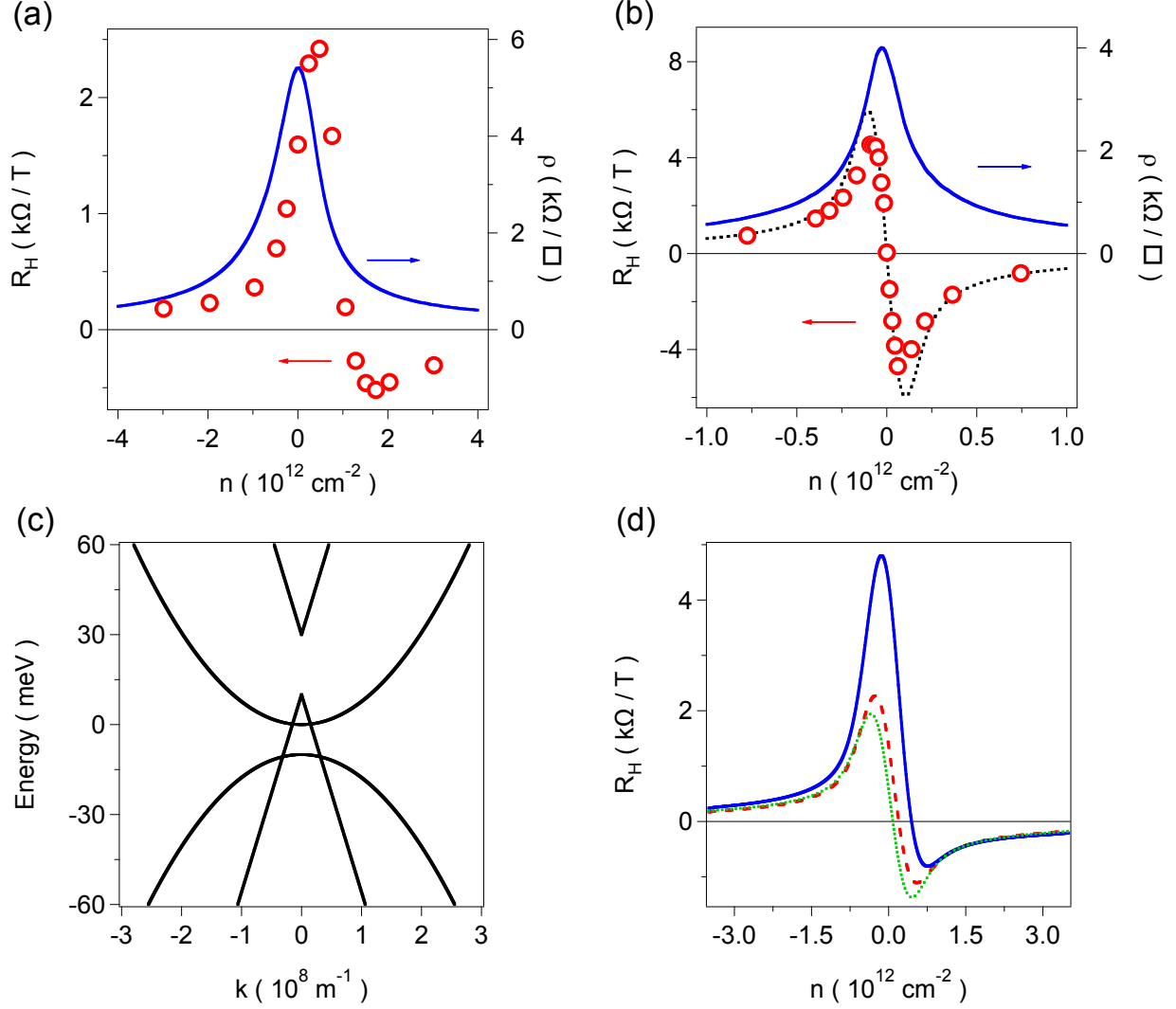


FIG. 5: (Color) (a) The low field Hall coefficient, R_H , and sheet resistivity, ρ , of ABA trilayer graphene as a function of n , for $D = 0$. Error bars are smaller than the symbol size. (b) R_H and ρ of monolayer graphene. The dotted line is $R_H = -1/ne$, averaged over disorder (see text). (c) Simplified ABA band structure. (d) R_H vs. n calculated for the band structure in (c), for mobility ratios $\mu_l/\mu_p = 3.3$ (solid blue), 1 (dashed red) and 0.3 (dotted green) (see text).